Journal of Materials Chemistry A

ROYAL SOCIETY OF CHEMISTRY

PAPER

View Article Online
View Journal | View Issue

Cite this: J. Mater. Chem. A, 2020, 8, 2033

The importance of the Mg–Mg interaction in Mg_3Sb_2–Mg_3Bi_2 shown through cation site alloying†

Max Wood, [a] Kazuki Imasato, [a] Shashwat Anand, [a] Jiong Yang [b] and G. Jeffrey Snyder *[a]

Received 14th October 2019
Accepted 20th December 2019

DOI: 10.1039/c9ta11328b

rsc.li/materials-a

Herein we study the effect alloying Yb onto the octahedral cite of Te doped $Mg_3Sb_{1.5}Bi_{0.5}$ has on transport and the material's high temperature stability. We show that the reduction in mobility can be well explained with an alloy scattering argument due to disrupting the $Mg_{octahedral}$–$Mg_{tetrahedral}$ interaction that is important for placing the conduction band minimum at a location with high valley degeneracy. We note this interaction likely dominates the conducting states across n-type Mg_3Sb_2–Mg_3Bi_2 solid solutions and explains why alloying on the anion site with Bi isn't detrimental to Mg_3Sb_2's mobility. In addition to disrupting this Mg–Mg interaction, we find that alloying Yb into the Mg_3Sb_2 structure reduces its n-type dopability, likely originating from a change in the octahedral site's vacancy formation energy. We conclude showing that while the material's figure of merit is reduced with the addition of Yb alloying, its high temperature stability is greatly improved. This study demonstrates a site-specific alloying effect that will be important in other complex thermoelectric semiconductors such as Zintl phases.

Introduction

Engineering defects are an important tool to improve the properties of a semiconductor, particularly a thermoelectric material.[1] Mg_3Sb_2 is a new thermoelectric material in which understanding and engineering its point defects was crucial to unlocking its potential as a good thermoelectric material.[2]

Mg_3Sb_2 was computationally suggested to be a good n-type thermoelectric material in 2013 (ref. 3) due to its high n-type valley degeneracy. While experimentalists were equipped with this information, they struggled to dope the material n-type due to persistent Mg vacancies on the Mg-1 octahedral cite, which would counteract any extrinsic n-type doping that was attempted.[2] Once this killer Mg vacancy defect was appreciated, experimentalists were able to counteract the killer defect by adding extra Mg to their samples to suppress the Mg vacancy formation and allow for extrinsic dopants to add electrons to the material.[4–9] Mg vacancies still readily form when samples are heated to temperatures above 400 °C,[10] due to the preferential sublimation of Mg from the sample.[11]

Mg_3Sb_2 can be thought of as a special case of the layered $CaAl_2Si_2$ (AB_2X_2) Zintl phase crystal structure in which the A and B sites are both composed of Mg, which we'll refer to as Mg(1) and Mg(2) respectively.[12] The Mg(2) site is tetrahedrally coordinated with Sb and forms the B_2X_2 layer. The Mg(1) site forms the intralayer site and is octahedrally coordinated with Sb atoms. Though Mg_3Sb_2 can be visualized through the layered $CaAl_2Si_2$ structure, Zhang *et al.* carefully showed the "layered" term may not be appropriate. This is because the Mg(1) and Mg(2) sites have similar Bader charge and bond strength with Sb, making the calculated material properties isotropic.[12]

While the term layered may not be apt for Mg_3Sb_2, the similar size and charges on Mg(1) and Mg(2) might play a role in why the material's electronic properties are unique within this crystal structure. Zhang *et al.* first pointed out that the conduction band minimum states of Mg_3Sb_2 are made out of Mg(1) s and Mg(2) s and p states.[9] Sun *et al.*, took this a step further and showed that the highly degenerate U* band ($N_v = 6$) was made up of covalent interactions between the Mg(1) and Mg(2) atoms.[13] This interaction can be demonstrated from first principles electronic structure and crystal orbital Hamilton population (COHP) calculations (see Fig. 1). The conduction band minima at the non high-symmetry U*-point lies in the Γ–A–L–M plane (see 2D Fermi-Energy contour plot in Fig. 2b). The k-resolved COHP for the conduction band in this 2D plane reveals Mg(1)s–Mg(2)s as the dominant interaction in the vicinity of U*-point. These conduction band states exhibit a significant bonding interaction between 3s levels of Mg(1) and Mg(2) as indicated by the negative values COHP values (see blue regions in Fig. 2) for states close to U*.

[a]Department of Materials Science and Engineering, Northwestern University, Evanston, Illinois 60208, USA. E-mail: jeff.snyder@northwestern.edu

[b]Materials Genome Institute, Shanghai University, 99 Shangda Road, Shanghai, 200444, China

† Electronic supplementary information (ESI) available. See DOI: 10.1039/c9ta11328b

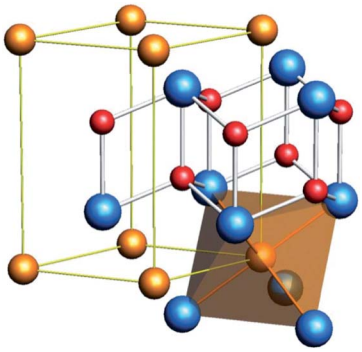

Fig. 1 Crystal structure of Mg_3Sb_2. Gold atoms represent the octahedrally coordinated Mg(1) atoms, red atoms represent the tetrahedrally coordinated Mg(2) atoms, and blue atoms represent Sb.

Sun went on to show that changing the octahedral site to another atom such as Yb or Ca computationally resulted in a more ionic interaction between the octahedral atom and the Mg_2Sb_2 layer. In these XMg_2Sb_2 compounds the conduction band minimum is moved to the higher symmetry M point ($N_v = 3$), which has less band degeneracy.[3,13,14]

Mg_3Sb_2 can form solid solutions with other compounds of the same crystal structure, with solubilities varying to differing degrees. Mg_3Bi_2 is commonly alloyed with Mg_3Sb_2 and is used to lower the material's lattice thermal conductivity and increase its weighted mobility.[15,16] Besides studies with Bi, Sun *et al.* calculated the valley degeneracy of Mg_3Sb_2, could be increased by alloying Yb or Ca onto the octahedral Mg site, moving the conduction band at U* up slightly in energy to be aligned with the band at M.[13]

Beyond this computational alloying study, there have been numerous papers published both computationally[17,18] and experimentally[9,19–21] testing the impact of different doping techniques. The main focus of which is the dopant's dopability (*i.e.* the maximum soluble amount of a dopant which donates charge carriers). However, in many of these dopant and alloying papers the type of states that make up the conduction band character is often overlooked. Disrupting these states can lead to additional short ranged potential scattering[22,23] or alloy scattering,[24] decreasing the materials performance.

Herein we investigate the properties of $Mg_{3.125-x}Yb_xSb_{1.5}Bi_{.5}Te_{0.01}$ and show a decrease in the mobility of the material as more Yb is added from disrupting the Mg(1)–Mg(2) interaction that make up the conduction band. Additionally, we show that this reduction can be well explained *via* an alloy scattering model. Finally, we show that while a sample's mobility is decreased, Yb alloying does benefit a sample's high temperature stability.

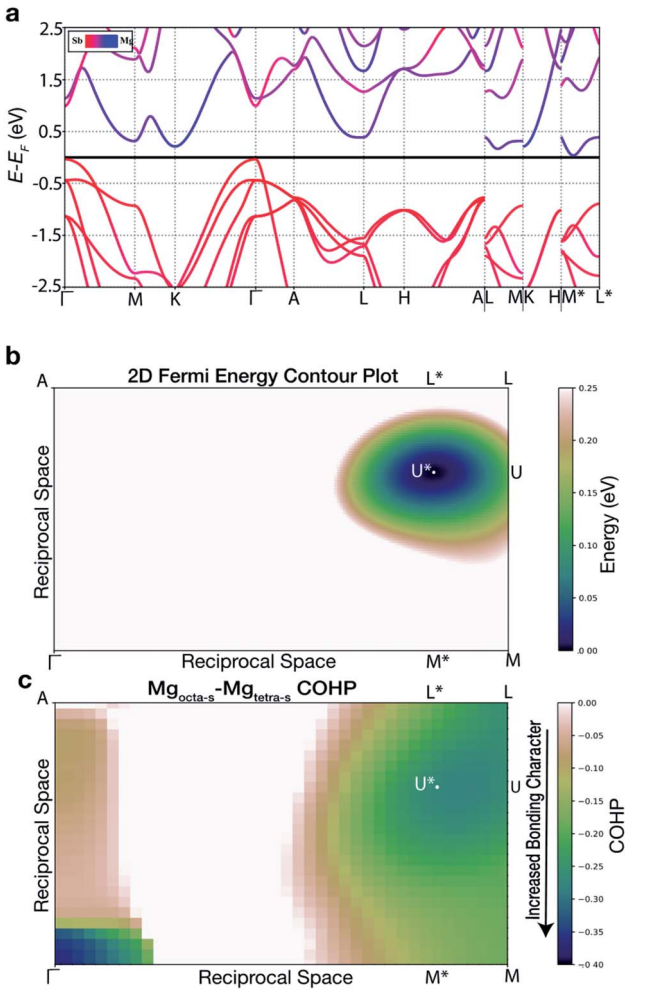

Fig. 2 (a) Atom-projected electronic band structure of Mg_3Sb_2. (b) Band energy contour plot up to 0.25 eV inside the conduction band for Mg_3Sb_2 in the Γ–A–L–M plane of the reciprocal space. (c) The k-resolved projected COHP for the interaction between Mg_{octa} and Mg_{tetra} in Mg_3Sb_2. The color scale varies over the COHP range [−0.4, 0] and saturating for positive values. This range of values was chosen to emphasize the presence of bonding interaction for states lying close to the conduction band minima.

Methods

First principles calculations

The density functional theory (DFT) calculation[25] in this study were performed using Vienna *ab initio* simulation package (VASP).[26] We have used Perdew–Burke–Ernzerhof (PBE) formulation of the exchange correlation energy functional derived under a gradient-generalized approximation (GGA).[27] Plane-wave basis sets truncated at a constant energy cutoff of 390 eV were used, as were Γ-centered k-point meshes with a density of ~8000 k-points per reciprocal atom (KPPRA). All structures were relaxed with respect to cell vectors and their internal degrees of freedom until forces on all atoms were less than 0.1 eV nm^{-1}. The k-resolved crystal orbital Hamilton populations (COHPs) calculations were performed using the version 3.2.0 of the LOBSTER software.[28–30]

Sample preparation

Samples of $Mg_{3.125-x}Yb_xSb_{1.4925}Bi_{0.4975}Te_{0.01}$ ($x = 0$, 0.075, 0.25, 0.4) were prepared *via* a high-energy ball mill using stoichiometric ratios of Mg turning (99.95% Alpha Aesar), Yb chunk (99.5% Alpha Aesar), Sb shot (99.999% 5N Plus), Bi shot (99.999% 5N Plus), Te shot (99.999% 5N Plus). Excess Mg was used in all samples in order to suppress the formation of

electron killing Mg vacancies. Starting elements were loaded into a steel ball milling vial in an argon dry glove box. Samples were then milled for 2 90 minute periods using a SPEX Sample Prep 800 Series Mixer/Mill. The powder from this milling process was consolidated using an induction heated rapid hot-press[31] under a flowing argon atmosphere within a 1/2 inch diameter high-density graphite die (POCO) into pellets approximately 1.5 mm in thickness. Samples were pressed at 800 °C for 20 minutes at 45 MPa. Resulting samples were found to have densities exceeding 95% theoretical densities.

Sample characterization

X-ray diffraction was performed on polished pellets using a STOE STADI MP with pure Cu Kα1 radiation in reflection geometry, followed by scanning electron microscopy with a Hitachi S-3400N-II. Densities of samples were measured geometrically and then confirmed with the Archimedes Principle. Resistivity and Hall coefficients were measured concurrently using a van der Pauw technique with pressure-assisted molybdenum contacts equipped with a 2T magnet.[32] Thermal diffusivity measurements were taken with a Netzsch LFA 457 under purged flowing argon, and the thermal conductivity was calculated using heat capacity from Agne *et al.*[33] Seebeck coefficient were measured under dynamic high vacuum with a homebuilt system using Chromel–Nb thermocouples.[34] All samples were investigated in pellet form with Seebeck and thermal diffusivity measured out of plane and resistivity and Hall coefficient being measured in the in-plane direction. The thermal stability of materials studied were measured *via* the change in Hall carrier concentration as a function of time at elevated temperatures.[10]

Results

X-ray diffraction

X-Ray Diffraction patterns for samples created of Mg_3Sb_2 alloyed with Bi and Yb and doped with Te are shown in Fig. S1 of the ESI.† From XRD we can identify no visible impurity phases. Fig. 3 shows the lattice parameters obtained from diffraction pattern of samples, with the dashed line showing the lattice parameters expected assuming a weighted average contribution from the four compounds that make up the solid solution. Both *a* and *c* rise linearly with increased Yb content up to $x = 0.25$, where beyond this composition the solubility of Yb into the structure has likely been exceeded. This is reflected by the $x = 0.4$ sample's lattice parameters deviating slightly from the predicted line. In addition to this evidence, energy dispersive spectroscopy (EDS) of the $x = 0.4$ and $x = 0.25$ samples (Fig. S3 and S4 in ESI†) shows no secondary phases precipitating out of the matrix, and a matrix composition that is within error of the respective samples' nominal compositions. Based on this data we can assume a solid solution is obtained at least until composition $x = 0.25$.

Transport

Table 1 shows how the Hall carrier concentration (defined as simply $1/R_H$, the Hall resistance) of Te doped $Mg_3Sb_{1.5}Bi_{0.5}$ is reduced as Yb is alloyed in. Additionally, Table 1 shows the Hall mobility and experimental density of states effective mass calculated from the Hall carrier concentration and Seebeck coefficient[39] for the samples that are unaffected by bipolar conduction. The $x = 0.2$ and $x = 0.4$ samples clearly show bipolar effects in both Seebeck and electrical conductivity so the actual free electron concentration is likely to be less than the measured n_H) There is barely an increase in effective mass observed to support the claim that adding Yb produces additional conducting states, however a benefit of these states to the materials' weighted mobility (Fig. 5) is not seen.

Thermoelectric transport studied (Fig. 4) follows a trend that is expected given the decreasing carrier concentration with Yb content. The Seebeck coefficient increases as Yb is alloyed is due to the reduction of carrier concentration, and the conductivity decreases. The thermal conductivity decreases with the addition of Yb, which is due in part to the reduction in the electronic portion of thermal conductivity. Additionally this decreasing trend can be attributed to a reduction in the lattice portion of thermal conductivity (Fig. S2†) as Yb is added due to a reduction in speed of sound computationally predicted[13] as well as alloy scattering of phonons.[40–44]

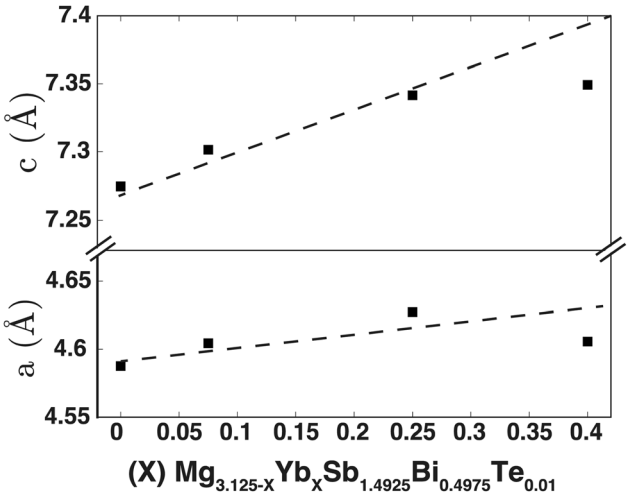

Fig. 3 Lattice parameters *a* and *c* for $Mg_{3.125-x}Yb_xSb_{1.5}Bi_{.5}Te_{0.01}$ samples determined from X-ray diffraction analysis. The dashed line is a projected lattice parameter given by a compositionally weighted fit of the lattice parameters of Mg_3Sb_2,[35] Mg_3Bi_2,[36] $YbMg_2Sb_2$,[37] and $YbMg_2Bi_2$ (ref. 38) taken from ICSD.

Table 1 Hall (n-type) carrier concentrations (n_H), Hall mobilities (μ_H), and density of states effective mass of samples $Mg_{3.125-x}Yb_xSb_{1.4925}Bi_{0.4975}Te_{0.01}$ created for this study measured at 400 K

X	n_H (cm^{-3})	μ_H ($cm^2\ V^{-1}\ s^{-1}$)	m^*_{DOS} (m_e)
0.0	2.4×10^{19}	90	1.1
0.075	2.3×10^{19}	55	1.1
0.25	1.7×10^{19}	~20	
0.4	9×10^{18}		

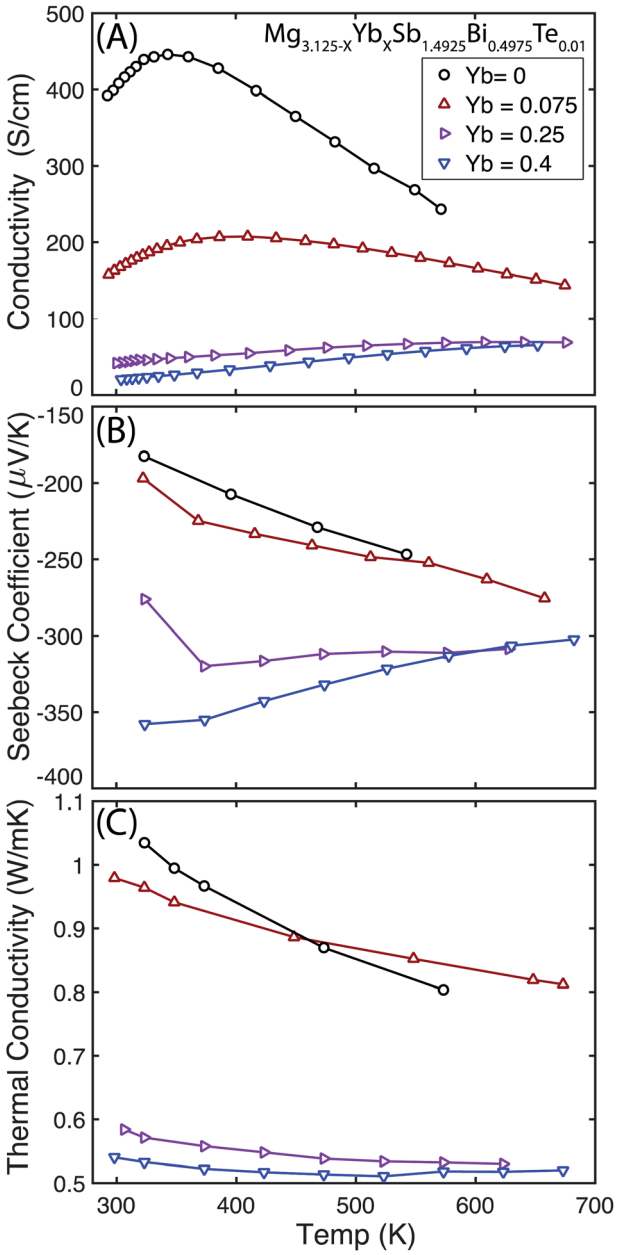

Fig. 4 (A) Conductivity, (B) Seebeck coefficient, and (C) thermal conductivity data for samples analyzed for this study.

Discussion

To compare transport in the samples we extracted the weighted mobility from a sample's Seebeck and conductivity data following.[39,45] Weighted mobility makes up the numerator of a materials quality factor and can be used to obtain a material's the peak power factor with changing carrier concentration.[22] As Yb is alloyed into the material we see a resulting decrease in its weighted mobility that follows the trend expected due to alloy scattering. As pointed out by Sun *et al.*[13] the Mg(1)–Mg(2) interaction is important in the electronic states at the conduction band minimum in Mg_3Sb_2. This explains why disrupting the Mg1 sites by replacing Mg with Yb has a large detrimental effect. This reduction in mobility is not seen[15,16] with alloying Bi on the anion site, which is expected because anions do not contribute much to the conduction band states.

To study the reduction in mobility in samples, an alloy scattering model is employed, which Wang *et al.* used to study the PbTe–PbSe alloy.[24] In this model we assume the total relaxation time of an electron is given by Matthiessen's rule such that:

$$\tau_{\text{total}}^{-1} = \tau_{\text{pure}}^{-1} + \tau_{\text{alloy}}^{-1}$$

or equivalently

$$\mu_{\text{total}}^{-1} = \mu_{\text{pure}}^{-1} + \mu_{\text{alloy}}^{-1}$$

where the scattering time from an alloy takes the form:

$$\tau_{0\,(\text{alloy})} = \frac{8\hbar^4}{3\sqrt{2}\pi\Omega x(1-x)U^2 m_b^{*3/2}(k_B T)^{1/2}}$$

in which Ω is the volume per atom, x is the concentration faction of the alloying atom, m_b^* is the density of states mass for a single band, and U is the alloy scattering potential.

While the initial compound is already an alloy of Mg_3Sb_2 and Mg_3Bi_2, we can separate Yb's contribution to alloy scattering by taking the 25% Mg_3Bi_2 as giving a "pure" weighted mobility. The reduction in weighted mobility due to alloy scattering therefore takes the form:

$$\mu_{w\,(\text{alloy})} = \mu_{0\,(\text{alloy})}\left(\frac{m_{\text{DOS}}^*}{m_e}\right)^{\frac{3}{2}} = \frac{8\hbar^4 N_v}{m_I^* 3\sqrt{2}\pi\Omega x(1-x)U^2 m_e^{*3/2}(k_B T)^{1/2}}$$

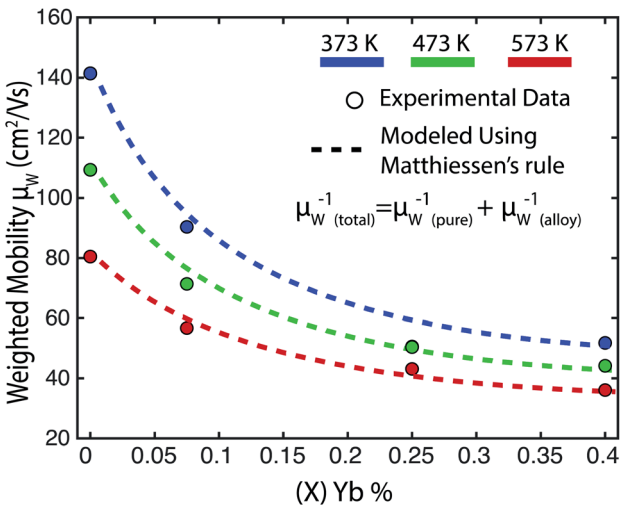

Fig. 5 Weighted mobility (μ_w) of samples *vs.* the Yb content at 373 K (blue), 473 K (green), and 573 K (red). Experimental values are given by data points. An alloy scattering model was employed to estimate the reduction in weighted mobility, (dashed lines). The alloy scattering potential term[24] U = 2.2 eV was used to estimate the reduction in weighted mobility.

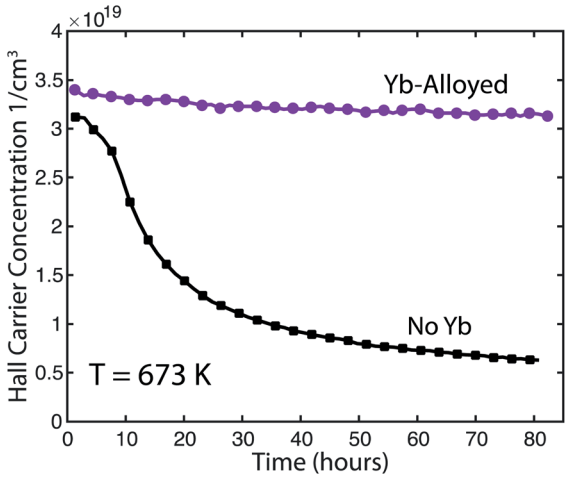

Fig. 6 Time dependency of the Hall carrier concentration of a Yb alloyed sample ($Yb_{0.75}Mg_{3.05}Sb_{1.4925}Bi_{0.4975}Te_{0.01}$) and a sample without Yb present ($Mg_{3.125}Sb_{1.4925}Bi_{0.4975}Te_{0.01}$) measured under dynamic vacuum that removed Mg vapor at 673 K.

where m^*_{DOS} is the density of states effective mass, m^*_I is the inertial effective mass and N_v is the degeneracy of the band(s) involved in transport. Using a $N_v = 6$ given by the degeneracy of the CB1 pocket, and using Zhang *et al.*'s calculated inertial masses isotropically averaged to $0.3m_e$ (ref. 46) we find an alloy scattering potential of 2.2 eV gives a curve matching the experimental data at a range of different temperatures (Fig. 5).

The reduction of carrier concentration as Yb is alloyed into the crystal is likely from cation site vacancies in the crystal, which have the effect of lowering the Te dopability in the alloy. Pomrehn *et al.* showed in AZn_2Sb_2 (A = Ca, Sr, Eu, Yb) as the A site was changed the vacancy formation energy of the A site also changed, with $YbZn_2Sb_2$ being the most susceptible to the formation of vacancies.[47] While the compound studied here contained Mg instead of Zn, the experimental data suggests a similar effect might exist as Yb is alloyed into Mg_3Sb_2.

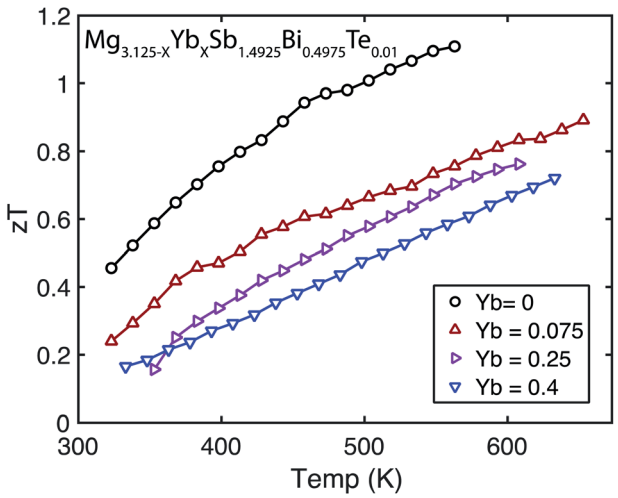

Fig. 7 zT of samples $Mg_{3.125-x}Yb_xSb_{1.4925}Bi_{0.4975}Te_{0.01}$.

While the mobility of Mg_3Sb_2 was decreased with alloying Yb, long term Hall tests (Fig. 6) show adding Yb appears to increase its high temperature stability. We speculate this change is due to a reduction of the diffusivity of Mg within the material after adding the larger Yb atom as it is also observed in a La-doping study.[10] Regardless of cause, this observed increased stability provides a possible route for Mg_3Sb_2 compounds to be used at higher temperatures.

The zT of the samples (Fig. 7) follows the same trend as weighted mobility with the zT decreasing with increasing Yb alloying. Yb alloying does decrease the lattice thermal conductivities of the samples studied, which is good for thermoelectric performance. However this decrease is not substantial enough to overcome the decrease in mobility from disrupting the Mg(1)–Mg(2) interaction.

Conclusion

In conclusion, alloying Yb on to the cation site of $Mg_{3.05}Sb_{1.4925}Bi_{0.4975}Te_{0.01}$ results in a reduction of the materials mobility due to alloy scattering. Alloying on the cation site appears to be detrimental not only because the conduction band is normally dominated by cations[23] but also because Yb disrupts the Mg(1)–Mg(2) interaction that is responsible for locating the conduction band minimum at the high valley degeneracy point U*. Although we see a reduction of zT with Yb alloy, the high temperature stability of the material increases with its addition.

When we compare anion site alloying with cation site alloying the importance of the Mg(1)–Mg(2) interaction becomes even more clear. Both cation site alloying with Yb and anion site alloying with Bi decreases thermal conductivity, and both alloying cases are predicted to create a band convergence effect should improve the weighted mobility. However the cation-site disorder disrupts the Mg(1)–Mg(2) interaction much more strongly than the anion-site disorder. Thus alloying on the anion site, which is less effected by the additional scattering, can benefit from the lower thermal conductivity and band convergence, producing higher zT.

Conflicts of interest

There are no conflicts to declare.

Acknowledgements

This work was supported by the NASA Science Mission Directorate's Radioisotope Power Systems Thermoelectric Technology Development. The IMSERC X-ray Facility at Northwestern University is supported by the Soft and Hybrid Nanotechnology Experimental (SHyNE) Resource (NSF ECCS-1542205); the State of Illinois and International Institute for Nanotechnology (IIN). Additionally this work was supported from acknowledge support from the "Designing Materials to Revolutionize and Engineer our Future" program of the National Science Foundation under Award No. 1729487.

References

1 Z. Li, C. Xiao, H. Zhu and Y. Xie, *J. Am. Chem. Soc.*, 2016, **138**, 14810–14819.
2 S. Ohno, K. Imasato, S. Anand, H. Tamaki, S. D. Kang, P. Gorai, H. K. Sato, E. S. Toberer, T. Kanno and G. J. Snyder, *Joule*, 2018, **2**(1), 141–154.
3 D. J. Singh and D. Parker, *J. Appl. Phys.*, 2013, **114**, 143703-7.
4 H. Tamaki, H. K. Sato and T. Kanno, *Adv. Mater.*, 2016, **28**, 10182–10187.
5 T. Kanno, H. Tamaki, H. K. Sato, S. D. Kang, S. Ohno, K. Imasato, J. J. Kuo, G. J. Snyder and Y. Miyazaki, *Appl. Phys. Lett.*, 2018, **112**, 033903-5.
6 J. Mao, Y. Wu, S. Song, J. Shuai, Z. Liu, Y. Pei and Z. Ren, *Materials Today Physics*, 2017, **3**, 1–6.
7 J. Mao, Y. Wu, S. Song, Q. Zhu, J. Shuai, Z. Liu, Y. Pei and Z. Ren, *ACS Energy Lett.*, 2017, **2**, 2245–2250.
8 J. Zhang, L. Song, S. H. Pedersen, H. Yin, L. T. Hung and B. B. Iversen, *Nat. Commun.*, 2017, **8**, 13901.
9 J. Zhang, L. Song, A. Mamakhel, M. R. V. Jørgensen and B. B. Iversen, *Chem. Mater.*, 2017, **29**, 5371–5383.
10 K. Imasato, M. Wood, J. J. Kuo and G. J. Snyder, *J. Mater. Chem. A*, 2018, **6**, 19941–19946.
11 M. Wood, J. J. Kuo, K. Imasato and G. J. Snyder, *Adv. Mater.*, 2019, e1902337, DOI: 10.1002/adma.201902337.
12 J. Zhang, L. Song, M. Sist, K. Tolborg and B. B. Iversen, *Nat. Commun.*, 2018, **9**, 4716.
13 X. Sun, X. Li, J. Yang, J. Xi, R. Nelson, C. Ertural, R. Dronskowski, W. Liu, G. J. Snyder, D. J. Singh and W. Zhang, *J. Comput. Chem.*, 2019, **40**, 1693–1700.
14 J. F. Sun and D. J. Singh, *J. Mater. Chem. A*, 2017, **5**, 8499–8509.
15 K. Imasato, S. D. Kang, S. Ohno and G. J. Snyder, *Mater. Horiz.*, 2018, **5**, 59–64.
16 K. Imasato, S. D. Kang and G. J. Snyder, *Energy Environ. Sci.*, 2019, **12**, 965–971.
17 P. Gorai, B. R. Ortiz, E. S. Toberer and V. Stevanović, *J. Mater. Chem. A*, 2018, **6**, 13806–13815.
18 P. Gorai, E. S. Toberer and V. Stevanović, *J. Appl. Phys.*, 2019, **125**, 025105-5.
19 S. W. Song, J. Mao, M. Bordelon, R. He, Y. M. Wang, J. Shuai, J. Y. Sun, X. B. Lei, Z. S. Ren, S. Chen, S. Wilson, K. Nielsch, Q. Y. Zhang and Z. F. Ren, *Materials Today Physics*, 2019, **8**, 25–33.
20 J. Zhang, L. Song, K. A. Borup, M. R. V. Jørgensen and B. B. Iversen, *Adv. Energy Mater.*, 2018, **8**, 1702776.
21 X. Shi, T. Zhao, X. Zhang, C. Sun, Z. Chen, S. Lin, W. Li, H. Gu and Y. Pei, *Adv. Mater.*, 2019, e1903387, DOI: 10.1002/adma.201903387.
22 H. Wang, Y. Pei, A. D. LaLonde and G. Jeffery Snyder, in *Thermoelectric Nanomaterials: Materials Design and Applications*, ed. K. Koumoto and T. Mori, Springer Berlin Heidelberg, Berlin, Heidelberg, 2013, pp. 3–32, DOI: 10.1007/978-3-642-37537-8_1.
23 H. Wang, X. Cao, Y. Takagiwa and G. J. Snyder, *Mater. Horiz.*, 2015, **2**, 323–329.
24 H. Wang, A. D. LaLonde, Y. Pei and G. J. Snyder, *Adv. Funct. Mater.*, 2013, **23**, 1586–1596.
25 W. Kohn, A. D. Becke and R. G. Parr, *J. Phys. Chem.*, 1996, **100**, 12974–12980.
26 G. Kresse and J. Furthmüller, *Phys. Rev. B*, 1996, **54**, 11169.
27 J. P. Perdew, K. Burke and M. Ernzerhof, *Phys. Rev. Lett.*, 1996, **77**, 3865.
28 S. Maintz, V. L. Deringer, A. L. Tchougréeff and R. Dronskowski, *J. Comput. Chem.*, 2013, **34**, 2557–2567.
29 V. L. Deringer, A. L. Tchougréeff and R. Dronskowski, *J. Phys. Chem. A*, 2011, **115**, 5461–5466.
30 R. Dronskowski and P. E. Blöchl, *J. Phys. Chem.*, 1993, **97**, 8617–8624.
31 A. D. LaLonde, T. Ikeda and G. J. Snyder, *Rev. Sci. Instrum.*, 2011, **82**, 025104-4.
32 K. A. Borup, J. de Boor, H. Wang, F. Drymiotis, F. Gascoin, X. Shi, L. D. Chen, M. I. Fedorov, E. Muller, B. B. Iversena and G. J. Snyder, *Energy Environ. Sci.*, 2015, **8**, 423–435.
33 M. T. Agne, K. Imasato, S. Anand, K. Lee, S. K. Bux, A. Zevalkink, A. J. E. Rettie, D. Y. Chung, M. G. Kanatzidis and G. J. Snyder, *Materials Today Physics*, 2018, **6**, 83–88.
34 S. Iwanaga, E. S. Toberer, A. LaLonde and G. J. Snyder, *Rev. Sci. Instrum.*, 2011, **82**, 063905-6.
35 M. Martinez-Ripoll, A. Haase and G. Brauer, *Acta Crystallogr., Sect. B: Struct. Crystallogr. Cryst. Chem.*, 1974, **30**, 2006–2009.
36 E. Wigner, *Z. Phys. Abtl. B-chem. Elem. Aufbau Mater.*, 1932, **19**, 203–216.
37 F. Wartenberg, C. Kranenberg, R. Pocha, D. Johrendt, A. Mewis, R.-D. Hoffmann, B. D. Mosel and R. Poettgen, *Z. Naturforschung B*, 2002, **57**, 1270–1276.
38 A. F. May, M. A. McGuire, D. J. Singh, R. Custelcean and G. E. Jellison Jr, *Inorg. Chem*, 2011, **50**, 11127–11133.
39 A. Zevalkink, D. M. Smiadak, J. L. Blackburn, A. J. Ferguson, M. L. Chabinyc, O. Delaire, J. Wang, K. Kovnir, J. Martin, L. T. Schelhas, T. D. Sparks, S. D. Kang, M. T. Dylla, G. J. Snyder, B. R. Ortiz and E. S. Toberer, *Appl. Phys. Rev.*, 2018, **5**, 021303-50.
40 J. Yang, G. P. Meisner and L. Chen, *Appl. Phys. Lett.*, 2004, **85**, 1140–1142.
41 M. Wood, U. Aydemir, S. Ohno and G. J. Snyder, *J. Mater. Chem. A*, 2018, **6**, 9437–9444.
42 B. Abeles, *Phys. Rev.*, 1963, **131**, 1906–19011.
43 P. G. Klemens, *Proc. Phys. Soc., London, Sect. A*, 1955, **68**, 1113–1128.
44 P. G. Klemens, *Phys. Rev.*, 1960, **119**, 507–509.
45 H. Wang, Y. Pei, A. D. LaLonde and G. J. Snyder, in *Thermoelectric Nanomaterials*, Springer, 2013, pp. 3–32.
46 J. Zhang and B. B. Iversen, *J. Appl. Phys.*, 2019, **126**, 085104-9.
47 G. S. Pomrehn, A. Zevalkink, W. G. Zeier, A. van de Walle and G. J. Snyder, *Angew. Chem., Int. Ed.*, 2014, **53**, 3422–3426.

